

## Article

# ZnO-Au Hybrid Metamaterial Thin Films with Tunable Optical Properties

Nirali A. Bhatt<sup>1</sup>, Robynne L. Paldi<sup>1</sup>, James P. Barnard<sup>1</sup> , Juanjuan Lu<sup>1</sup>, Zihao He<sup>2</sup>, Bo Yang<sup>1</sup> , Chao Shen<sup>1</sup>, Jiawei Song<sup>1</sup>, Raktim Sarma<sup>3</sup>, Aleem Siddiqui<sup>3</sup> and Haiyan Wang<sup>1,2,\*</sup> 

- <sup>1</sup> School of Materials Engineering, Purdue University, West Lafayette, IN 47907, USA; bhatt8@purdue.edu (N.A.B.); rpaldi@purdue.edu (R.L.P.); barnardj@purdue.edu (J.P.B.); lu790@purdue.edu (J.L.); yang837@purdue.edu (B.Y.); shen569@purdue.edu (C.S.); song675@purdue.edu (J.S.)
- <sup>2</sup> School of Electrical and Computer Engineering, Purdue University, West Lafayette, IN 47907, USA; he468@purdue.edu
- <sup>3</sup> Sandia National Laboratory, Albuquerque, NM 87123, USA; rsarma@sandia.gov (R.S.); asiddiq@sandia.gov (A.S.)
- \* Correspondence: hwang00@purdue.edu

**Abstract:** ZnO-Au nanocomposite thin films have been previously reported as hybrid metamaterials with unique optical properties such as plasmonic resonance properties and hyperbolic behaviors. In this study, Au composition in the ZnO-Au nanocomposites has been effectively tuned by target composition variation and thus resulted in microstructure and optical property tuning. Specifically, all the ZnO-Au nanocomposite thin films grown through the pulsed laser deposition (PLD) method show obvious vertically aligned nanocomposite (VAN) structure with the Au nanopillars embedded in the ZnO matrix. Moreover, the average diameter of Au nanopillars increases as Au concentration increases, which also leads to the redshifts in the surface plasmon resonance (SPR) wavelength and changes in the hyperbolic behaviors of the films. As a whole, this work discusses how strain-driven tuning of optical properties and microstructure resulted through a novel Au concentration variation approach which has not been previously attempted in the ZnO-Au thin film system. These highly ordered films present great promise in the areas of sensing, waveguides, and nanophotonics to name a few.

**Keywords:** hyperbolic metamaterials; surface plasmon resonance; vertically aligned nanocomposites; strain-driven tuning



**Citation:** Bhatt, N.A.; Paldi, R.L.; Barnard, J.P.; Lu, J.; He, Z.; Yang, B.; Shen, C.; Song, J.; Sarma, R.; Siddiqui, A.; et al. ZnO-Au Hybrid Metamaterial Thin Films with Tunable Optical Properties. *Crystals* **2024**, *14*, 65. <https://doi.org/10.3390/cryst14010065>

Academic Editors: Antonio Del Bosque and Xoan Xosé Fernández Sánchez-Romate

Received: 30 November 2023

Revised: 3 January 2024

Accepted: 3 January 2024

Published: 6 January 2024



**Copyright:** © 2024 by the authors. Licensee MDPI, Basel, Switzerland. This article is an open access article distributed under the terms and conditions of the Creative Commons Attribution (CC BY) license (<https://creativecommons.org/licenses/by/4.0/>).

## 1. Introduction

Zinc Oxide (ZnO), though relatively new in the field of nanotechnology, has historical uses dating back centuries such as in ointments and watercolor pigment [1,2]. Recently, it is widely used in various industries and applications, such as rubber tire production [3], mineral sunscreens to protect against UV-A radiation [4], therapeutics because of its anti-cancer, anti-bacterial, and antioxidant properties [5], textiles [5], and agriculture [5] to name a few. The fabrication of ZnO nanostructures grown using thermal processing in 2001 has opened a new direction for ZnO [6]. From then on, many other 1-D ZnO nanostructures have been developed [7], forming because of the noncentral symmetry and polarity in the ZnO wurtzite hexagonal crystal structure [7,8]. ZnO also holds multiple unique properties which have made it an oxide of increased interest, including wide band gap semiconductor, piezoelectric [9] and pyroelectric [10] behavior. It is also a transparent conductive oxide [11], with good radiation hardening resistance properties [10], and is nontoxic [12], biodegradable [13], and biocompatible [13].

Mixing metallic nanostructures into ZnO as ZnO-based nanocomposites has drawn great research interests in enhancing its multifunctionalities, such as Au for enhanced surface plasmon resonance properties and catalytical properties. Very recently, thin film

approaches have been used to grow metal-ZnO nanocomposites with uniform metal distributions. Specifically, two types of metal morphologies have been achieved, i.e., particle in matrix (PIM) and vertically aligned nanocomposite (VAN), with PIM being more common in oxide-metal growths. In PIM, the metal presents itself as nanoparticles which are evenly distributed in the oxide matrix [14]. Noble metals such as Au, Pt, and Ag have been grown as nanoparticles and researched due to their unique optical properties, specifically the localized surface plasmon resonance (LSPR) response they demonstrate [15]. The shape, size, and dispersion of these metal nanoparticles in the matrix they are in can tune this LSPR phenomenon thus giving them a variety of possible applications [15–18]. VAN on the other hand, is when metallic nanopillars are self-assembled epitaxially in the oxide matrix on a substrate [14,19]. VAN are uniquely advantageous because the functionality of the films can be tuned through material selection and as a result, vertical strain can be tuned and controlled [19,20]. Oxide-metal VAN are able to tune not only the LSPR phenomenon but also epsilon near zero (ENZ) permittivity thereby varying the hyperbolic dispersion of hyperbolic metamaterials [HMM] [21–26].

These well controlled thin film-based nanocomposites also demonstrated powerful tunability in optical properties. For example, ZnO-Au-based VAN films grown via pulsed laser deposition (PLD) process have shown effective tuning via oxygen pressure and laser frequency [27], and alloying with other metals [26]. In this work, we explore the power of Au composition on the tuning of ZnO-Au nanocomposite thin films. Such composition tuning has been achieved by the target composition variation from 10%, 20% to 30% of Au. Detailed microstructural characterizations were carried out to compare the effects of Au composition on the overall epitaxial growth quality, morphology and distribution of Au nanostructures and strain coupling effects. Optical properties including plasmonic resonance properties and optical anisotropy have been explored using UV-vis transmittance measurements and ellipsometry measurements.

## 2. Materials and Methods

### 2.1. Thin Film Growth

All of the ZnO-Au VAN thin films which include the ZnO plus 10% mol Au, 20% mol Au, and 30% mol Au (overall mol% of Au are written in Table S1 and the resulting composition after film deposition is seen in Figure S1), were grown using pulsed laser deposition (PLD). All films were deposited on c-cut sapphire substrates with a KrF excimer laser ( $\lambda = 248$  nm) using 3 different ZnO-Au composite targets. All the ZnO-Au composite targets were processed using the spark plasma sintering process. Deposition conditions included a substrate temperature of 610 °C, target-substrate distance of 4.5 cm, laser frequency of 5 Hz, oxygen background pressure of 20 mTorr, and laser energy of 420 mJ. Before deposition, the base pressure was  $3 \times 10^{-6}$  Torr or better.

### 2.2. Microstructure Characterization

Microstructure characterization was conducted using X-ray diffraction (XRD), transmission electron microscopy (TEM), scanning transmission electron microscopy (STEM), scanning electron microscope, and energy-dispersive X-ray spectroscopy (EDS). A Malvern PANalytical Empyrean X-ray diffractometer (XRD) from Worcestershire, UK was used to conduct  $\theta - 2\theta$  scans with Cu  $K_{\alpha}$  ( $\lambda = 0.154$  nm) radiation. The TEM/STEM/EDS-mapping images were taken using the ThermoFisher TALOS F200X TEM. The cross-section TEM samples were prepared by a standard sample preparation procedure consisting of manual grinding, dimple polishing, and ion milling (PIPS 695 system, 5keV). The SEM BSE (backscattered electron) images were taken using the Teneo Volumescape SEM.

### 2.3. Optical Measurements

Optical measurements were obtained using a J.A. Woollam RC2 spectroscopic ellipsometer for ellipsometry measurements. A B-spline model coupled with a uniaxial model

were applied to get optical permittivity measurements in the range of 210–2500 nm. A Lambda 1050 UV-vis spectrophotometer was used for transmittance (%T) measurements.

### 3. Results

#### 3.1. XRD

X-ray diffraction data were collected to examine the growth quality and phase composition of various ZnO-Au VAN films. Figure 1a shows the  $\theta$ - $2\theta$  plots collected for all the samples. Highly textured growth is obviously seen with the preferred out of plane direction of ZnO (0002) and Au (111) on  $\text{Al}_2\text{O}_3$  (0006). This relationship helps explain the connection between the dissimilar crystal structures of ZnO and Au. ZnO has a hexagonal closed packed structure while Au has a face centered cubic (FCC) structure. Thus ZnO (001) grows well on  $\text{Al}_2\text{O}_3$  (0006), while Au (111) with a 3-fold symmetry matches to  $\text{Al}_2\text{O}_3$  (0006) [27].

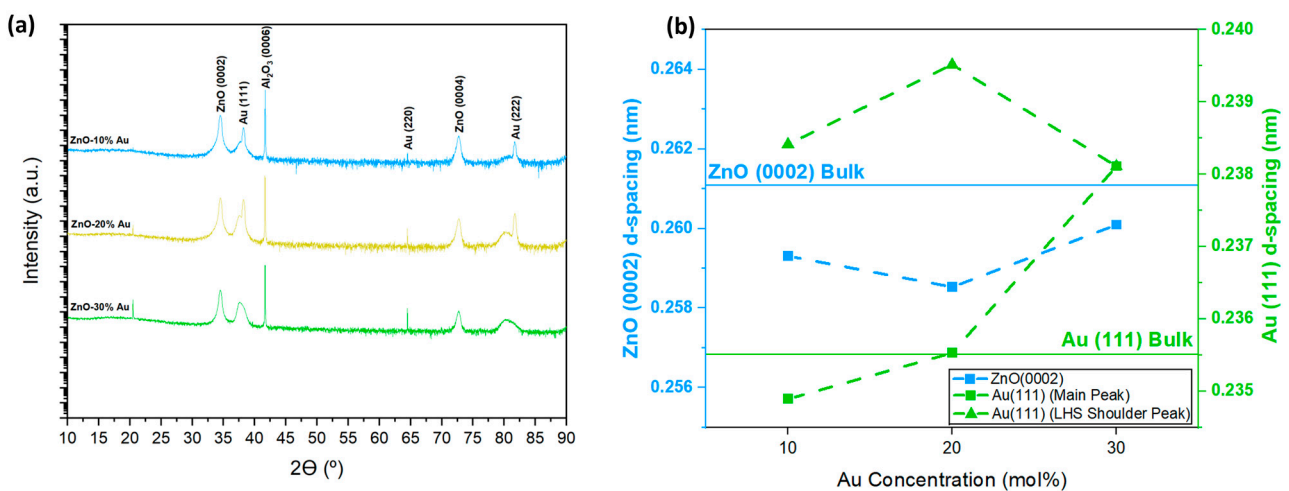


**Figure 1.** (a) XRD  $\theta$ - $2\theta$  scans for the different gold composition films and (b) the corresponding d-spacing plot of ZnO (0002) and Au (111). (b) shows the d-spacing of the main Au (111) and the left shoulder peak on the Au (111) especially for the 10% and 20% Au samples.

The calculated d-spacing values for ZnO (0002) and Au (111) are plotted in Figure 1b for all three ZnO-Au samples. The blue and green solid lines are the bulk d-spacing values of ZnO (0002) and Au (111), respectively, as reference. The green square line represents the d-spacing for the main Au (111) peak while the green triangle line represents the d-spacing for the left-hand side (LHS) shoulder peak especially for the 10% and 20% Au samples. Error values for the d-spacing are as follows:  $\pm 0.1$  nm for the ZnO (0002) peak and  $\pm 0.1$  nm for the Au (111) peak.

In general, Au (111) main peak d-spacing values increase as the Au concentration increases while ZnO (0002) d-spacings remain comparable with a minor increase. Specifically, in the 10% Au film, both Au (111) and ZnO (0002) are under compression. When the Au concentration increases to 20% Au, ZnO is still under compression while the Au is nearly the same as the bulk value. Finally, in the sample with 30% Au, the ZnO is under compression and the Au is now in tension. Considering the interfacial strain coupling along the vertical interfaces in ZnO-Au VAN thin films, Au (111) will be under tensile strain while ZnO (0002) is expected to be under compressive strain. This is consistent with the strain results in the 30% Au sample. It is noted that Au (111) has experienced a larger strain variation than that of ZnO suggesting the Au pillars are more likely to be tensile strained by the ZnO matrix. Overall, the texture relationship is ZnO (0002) || Au (111) ||  $\text{Al}_2\text{O}_3$  (0006).

Additionally, the Au (111) peak in Figure 1a shows a left shoulder peak for the 10% and 20% Au samples. The d-spacing of the shoulder peak has been calculated and plotted

as the green triangle line found in Figure 1b. Unlike the main peak, this Au (111) shoulder peak is in tension for all Au concentrations. This can be attributed to the morphology of the films. Specifically, the 10% and 20% Au samples have both particle and pillar morphology, leading some of the Au to be strain coupled to the substrate while the main Au (111) peak is strain coupled to the ZnO matrix. The Au (111) peak in the ZnO-30%Au sample shifts to a smaller angle and is broadened. This could be attributed to the large amount of Au present in the film and the resulting lattice distortion and inhomogeneity in composition, as previously reported [28]. The same reasoning can be applied to the visibly broadened and shifted Au (222) peak.

### 3.2. Microstructure

STEM along with EDS mapping was conducted and summarized in Figure 2 to explore the microstructure variation as a function of the Au concentration. All the films were grown to be of comparable thicknesses (~80 nm). It is obvious that all the samples show clear vertical Au nanopillars throughout the film thickness, with increasing pillar density and diameters as the Au composition increases from 10% to 30%. The 10% and 20% samples also show more discontinued Au nanopillars, while the 30% one shows more straight and continuous pillars. The Au nanopillar diameters are plotted in Figure 3 for all three samples. The average pillar diameter is 2.3 nm, 3.7 nm, and 5.0 nm for the 10%, 20% and 30% Au films, respectively. This tuning of the pillar diameter with Au content variation is what gives these ZnO-Au films the unique tunable optical properties discussed next.

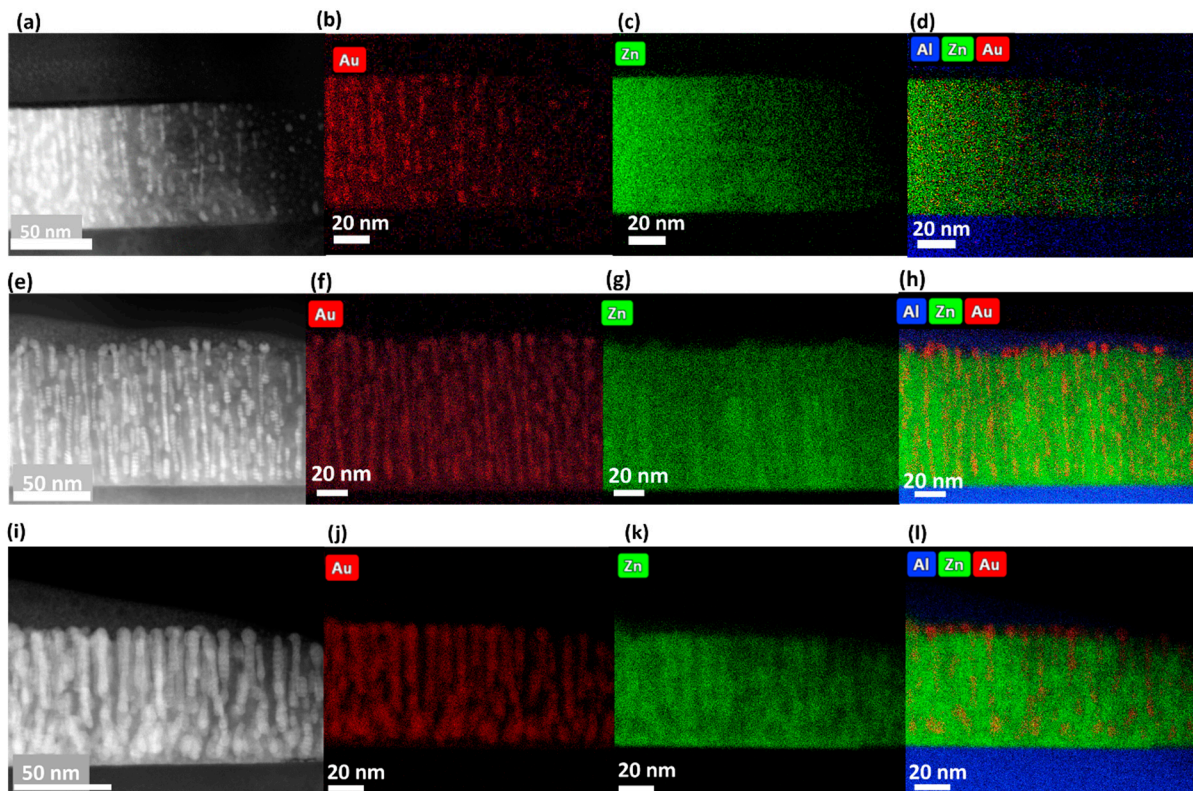


**Figure 2.** Microstructure characterization of the Au concentration tuning. (a) Cross-section STEM and (b) Au, (c) Zn, (d) combined EDS mapping image of the ZnO-10% Au film. (e) Cross-section STEM and (f) Au, (g) Zn, (h) combined EDS mapping image of the ZnO-20% Au film. (i) Cross-section STEM and (j) Au, (k) Zn, (l) combined EDS mapping image of the ZnO-30% Au film.

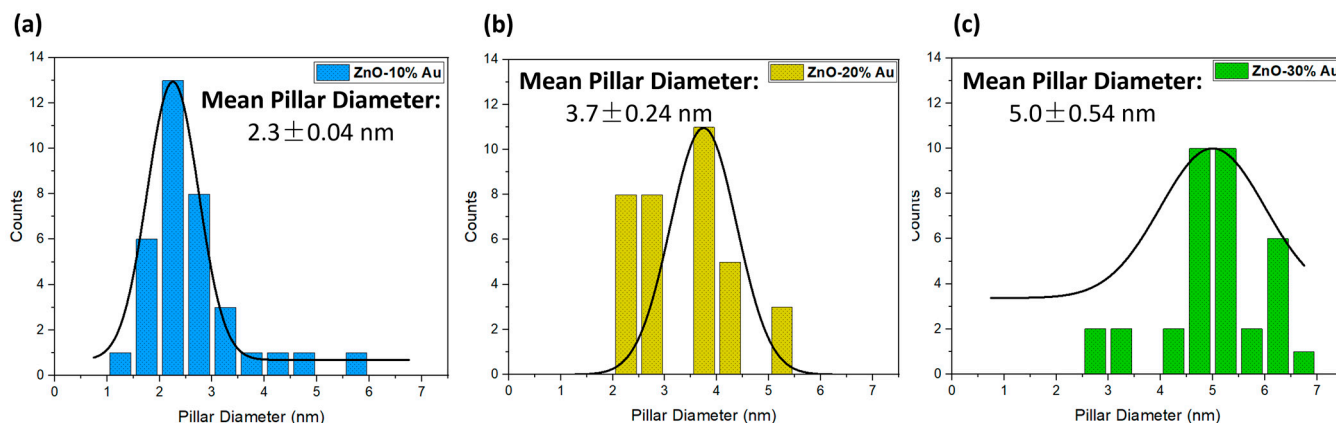


**Figure 3.** Histogram of pillar diameters of (a) ZnO-10% Au, (b) ZnO-20% Au, and (c) ZnO-30% Au films. The mean pillar diameter is stated in each image.

### 3.3. Optical Properties

Considering the plasmonic properties of Au nanostructures, UV-vis transmittance measurements were conducted on the Au-ZnO VAN thin films with different Au compositions. Figure 4 shows the transmittance plots as a function of wavelength in the range of 210 nm to 750 nm for all the samples. By comparing the data for the 10% Au, 20% Au, and 30% Au films, there is an obvious redshift of the surface plasmon resonance peak as the Au concentration increases, as labelled as arrows. Specifically, the ZnO-10% Au film shows a plasmonic resonance response at 510 nm, the ZnO-20% Au film shows a plasmonic resonance response at 513 nm, and the ZnO-30% Au film shows a plasmonic resonance response at 545 nm. Such larger redshift of the plasmon resonance peak from the 10% and 20% Au to the 30% Au is likely related to the thicker, well-formed Au nanopillars in the 30% Au sample (~5.0 nm in average pillar diameter). There is also a broadening of the absorption edge as this redshift occurs possibly due to the broadening of the diameter distribution of the Au nanopillars in the 30% Au film. Moreover, there is a decrease in %T as the Au content increases, suggesting the film allows less light through which can be attributed to the increased Au content as well as the increased pillar size. Additionally, the SPR wavelength can be tuned by the aspect ratio of the Au nanopillars. Therefore, another reason for the redshift in SPR wavelength as the Au content increases is the better formation of continuous Au pillars. As the pillars become more continuous and have larger diameters, the proximity of one Au pillar to the next decreases. This smaller interpillar distance leads to better near-field plasmonic coupling thus the observed redshift as the microstructure changes [29]. Such redshift in ZnO-Au films has also been previously reported when background oxygen pressure has been varied which results in more randomized Au pillars growing in the VAN [27]. Additionally, increasing the laser frequency led to an increase in Au pillars resulting in a redshift of the SPR wavelength [27]. In this work, the redshift can be attributed to the increase in ordering and average pillar diameters as a result of increasing the Au concentration in the films. This suggests that Au concentration tuning in the films can effectively tune the SPR response in addition to the previously reported deposition parameter variation. Sensing is one of the most widely used applications of the SPR phenomenon in Au nanopillars [30]. Since the size and shape of the Au nanopillar can tune the SPR wavelength, light sensing can be detected due to the dip in light intensity corresponding to the resonant frequency of the Au structure. The refractive index of the matrix surrounding the Au nanopillars can also tune the SPR wavelength as well. Optical sensing is clearly a promising area for the use of these kinds of films.

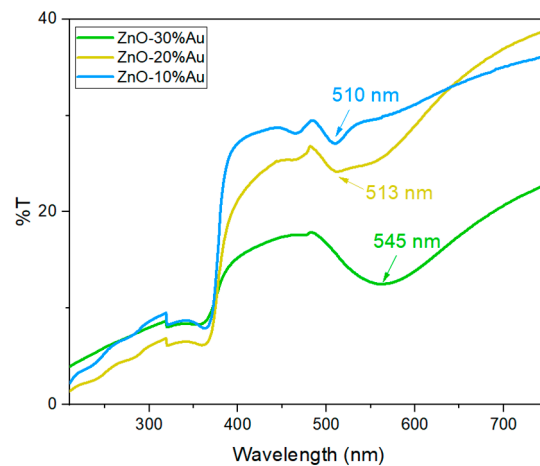


**Figure 4.** UV-Vis transmission (%T) of the ZnO-Au films with varying gold concentration. The numerical values listed in the plot represent the wavelength corresponding to the surface plasmonic resonance response of the individual films.

Due to the fact that these films were composed of an oxide and a metal, hyperbolic behavior (when the film behaves like a dielectric in one direction and a metal in the other for a given range of wavelengths) was expected. To understand this hyperbolic dispersion and optical permittivity for the films with different Au compositions, spectroscopic ellipsometry measurements were conducted. A B-Spline model was used to fit the film thickness and achieve a mean square error of less than 5. A uniaxial model was used to fit the data to understand the in and out-of-plane permittivities. All the samples demonstrate evident hyperbolic dispersion and ENZ (epsilon near zero) values. These 3 films are ZnO-30%Au, ZnO-20%, and ZnO-10% films. The ZnO-30% Au film shows 2 hyperbolic regions and two ENZ points in the out of plane direction.

For the ZnO-10% Au thicker film in Figure 5a, the optical permittivity data presents 3 ENZ values at 234 nm, 279 nm, and 2118 nm all in the in-plane direction. In the regions between 234–279 nm and greater than 2118 nm, the in-plane component ( $\epsilon_{//}$ ) is negative while the out-of-plane component ( $\epsilon_{\perp}$ ) is positive. This means that in these regions, the film behaves Type II hyperbolic structure, i.e., a metallic manner in-plane while a dielectric out-of-plane. For the ZnO-20% Au thicker film in Figure 5b, there is one ENZ value at 1115 nm in the out-of-plane direction. In the region between 1115–2500 nm,  $\epsilon_{\perp}$  is negative while  $\epsilon_{//}$  is positive. This suggests a Type I hyperbolic structure, i.e., metallic behavior in out of plane direction and a dielectric in-plane. For the ZnO-30% Au film seen in Figure 5c, there are two ENZ values at 339 nm and 693 nm in the out-of-plane direction. In the regions between 210–339 nm and 693–2500 nm, the film behaves as a Type I hyperbolic structure, i.e., a metal out-of-plane and a dielectric in-plane. The variability in the hyperbolic dispersion and ENZ values of these films is an outcome of the anisotropic nature of the ZnO-Au VAN and consequently of the amount of Au in the films. HMMs can actually improve the SPR sensing capability in devices [31]. Therefore, hyperbolic dispersion dips can be attributed to surface plasmon resonance. The slight dip in Figure 5a around 500 nm can be attributed to the SPR dip for the 10% Au film seen in Figure 4. Applications of HMMs include waveguides, hyperlenses, and sensors [32].

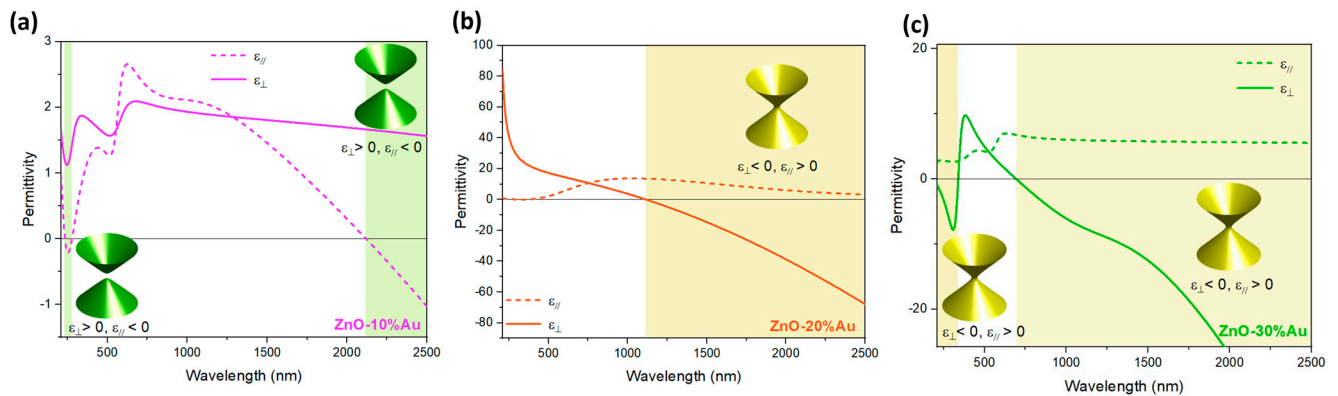


**Figure 5.** Real part of the optical permittivity of the (a) ZnO–10% Au Thicker, (b) ZnO–20% Au Thicker, and (c) ZnO–30% Au films. The regions where hyperbolic dispersion is present are highlighted. The green region corresponds to the green hyperboloid of two sheets while the yellow region corresponds to the yellow hyperboloid of one sheet.

#### 4. Discussion

One advantage of Au composition tuning is the ability to grow high quality films regardless of Au content up to 30 mol %. This is evidenced from the strong Au (111) XRD peaks for the different samples. This is in contrast to the films grown with individual Zn and Au targets through sputtering which demonstrated a decrease in Au (111) XRD peak intensity with Au content increase [33], which also lead to the degradation of the crystallinity of the ZnO and Au isolating and clustering in the films. Additionally, tuning the Au concentration also allows the pillar diameter tuning from 2.3 nm to 5.0 nm for 10% and 30% Au, respectively. In comparison, tuning laser frequency has shown to result in a larger range and larger sized pillars with diameters ranging from 15 nm to 27 nm [27]. Additionally, the use of low Au composition to achieve smaller Au pillars is a more economic option compared to the 1:1 ratio ZnO/Au nanocomposite targets used previously [27].

Surface plasmon resonance tuning has been also observed in this work and the prior work on laser frequency tuning [27]. In this work, Au concentration tuning results in the absorption edge broadening when there are more Au nanopillars present. Interestingly, plasmon resonance dips occur at varying wavelengths for the laser frequency study and the Au concentration tuning study. Specifically, the Au concentration tuning method shows SPR dips in the wavelengths ranging from 510 nm to 545 nm while the films grown through varying laser frequency show SPR dips in the wavelengths ranging from 573 nm to 600 nm [27]. In both cases, there is a redshift of the SPR wavelengths, but the cause is different. When the Au concentration in the film increases, there is a redshift in SPR wavelengths corresponding to an increase in Au pillar diameter and a more pillar like morphology of the Au in the film. When the laser frequency increases, there is a redshift in SPR wavelengths corresponding to a decrease in Au pillar diameter but an increase in the number of pillars [27].

These highly ordered ZnO-based VAN films present great promise in the areas of sensing [34], waveguides [34], and nanophotonics [35] just to name a few. Future research in regard to Au concentration variation in ZnO-Au VAN could continue in the areas of complex multilayer films with different Au concentrations or different ZnO-metal VANs. Additionally, considering the minute magnetic properties in ZnO, a study on magnetic and plasmonic coupling properties in ZnO-Au VANs and other ZnO-magnetic metal VANs could be conducted. Plus, a further look at the tunability of the nonlinearity and second harmonic generation (SHG) can be conducted. Preliminary SHG data are shown in Figure S2 though no obvious SHG was observed. (In Supplementary Materials)

## 5. Conclusions

In this work, The ZnO-Au VAN thin films with different Au composition varied from 10%, 20% to 30% have been deposited and their microstructure and properties have been compared. The Au concentration tuning in these ZnO-Au VAN films has led to Au nanopillar morphology tuning, strain variation, and the tuning of SPR properties and hyperbolic dispersion. The ZnO-30% Au films show better developed and thicker Au VAN pillars compared to the 10% and 20% samples. The SPR showed a redshift in wavelength with the formation of more structured and thicker Au pillars as the Au concentration increases. All the samples show clear hyperbolic behavior with different epsilon near-zero (ENZ) values and hyperbolic dispersion regions in relation to Au concentration. Au composition tuning has been demonstrated as an effective approach for tuning microstructure and properties in ZnO-Au VAN hybrid metamaterials for future applications in integrated photonic devices and optical sensors.

**Supplementary Materials:** The following supporting information can be downloaded at: <https://www.mdpi.com/article/10.3390/cryst14010065/s1>, Table S1: Table of the actual mol% of Au in the composite ZnO-Au target, Figure S1: Table showing composition from EDS mapping, Figure S2: Initial second harmonic generation (SHG) measurements for the ZnO+30%mol Au film, Figure S3: Backscattered electron (BSE) SEM images of the (a) 10% Au, (b) 20% Au, and (c) 30% Au samples. The bright contrast spots are the Au while the gray contrast area is the ZnO.

**Author Contributions:** Conceptualization, Investigation, Methodology, writing—Original Draft, writing—review and editing, N.A.B.; Investigation, writing—review and editing, R.L.P., J.P.B., J.L., Z.H., B.Y., C.S. and J.S.; Funding acquisition, supervision, writing—review and editing, R.S. and A.S.; Conceptualization, Funding Acquisition, Supervision, Writing—Review and Editing, H.W. All authors have read and agreed to the published version of the manuscript.

**Funding:** This work is supported by the U.S. Department of Energy, Office of Science, Basic Energy Sciences under Award DE-SC0020077. This work was also partially supported by the Laboratory Directed Research and Development program at Sandia National Laboratories, a multimission laboratory managed and operated by National Technology and Engineering Solutions of Sandia, LLC., a wholly owned subsidiary of Honeywell International, Inc., for the U.S. Department of Energy's National Nuclear Security Administration under contract DE-NA-003525. Additionally, this work was supported by the Sandia National Laboratories Diversity Initiative Fellowship. The high-resolution STEM work was supported by the U.S. National Science Foundation DMR-2016453. The target preparation effort was supported by the U.S. Office of Naval Research N00014-22-1-2160 and N00014-20-1-2043.

**Data Availability Statement:** Data are contained within the article or supplementary material.

**Acknowledgments:** N.A.B. thanks the support from the Purdue University Andrews Graduate Fellowship. N.A.B. and R.L.P. acknowledge the support from the Sandia Diversity Fellowship Program from Sandia National Laboratory. This work was performed under the Laboratory Directed Research and Development (LDRD) program at Sandia National Laboratories. Sandia National Laboratories is a multimission laboratory managed and operated by National Technology & Engineering Solutions of Sandia, LLC, a wholly owned subsidiary of Honeywell International Inc., for the U.S. Department of Energy's National Nuclear Security Administration under contract DE-NA0003525. This paper describes objective technical results and analysis. Any subjective views or opinions that might be expressed in the paper do not necessarily represent the views of the U.S. Department of Energy or the United States Government.

**Conflicts of Interest:** The authors declare no conflicts of interest. The funders had no role in the design of the study; in the collection, analyses, or interpretation of data; in the writing of the manuscript, or in the decision to publish the results.

## References

1. Frederickson, C.J.; Koh, J.-Y.; Bush, A.I. The Neurobiology of Zinc in Health and Disease. *Nat. Rev. Neurosci.* **2005**, *6*, 449–462. [[CrossRef](#)] [[PubMed](#)]
2. Borysiewicz, M.A. ZnO as a Functional Material, a Review. *Crystals* **2019**, *9*, 505. [[CrossRef](#)]

3. Paulthangam, K.M.; Som, A.; Ahuja, T.; Srikrishnarka, P.; Nair, A.S.; Pradeep, T. Role of Zinc Oxide in the Compounding Formulation on the Growth of Nonstoichiometric Copper Sulfide Nanostructures at the Brass–Rubber Interface. *ACS Omega* **2022**, *7*, 9573–9581. [[CrossRef](#)] [[PubMed](#)]
4. Smijs, T. Pavel Titanium Dioxide and Zinc Oxide Nanoparticles in Sunscreens: Focus on Their Safety and Effectiveness. *Nanotechnol. Sci. Appl.* **2011**, *4*, 95–112. [[CrossRef](#)]
5. Sharma, P.; Hasan, M.R.; Mehto, N.K.; Deepak; Bishoyi, A.; Narang, J. 92 Years of Zinc Oxide: Has Been Studied by the Scientific Community since the 1930s– An Overview. *Sens. Int.* **2022**, *3*, 100182. [[CrossRef](#)]
6. Pan, Z.W.; Dai, Z.R.; Wang, Z.L. Nanobelts of Semiconducting Oxides. *Science* **2001**, *291*, 1947–1949. [[CrossRef](#)] [[PubMed](#)]
7. Wang, Z.L. Nanostructures of Zinc Oxide. *Mater. Today* **2004**, *7*, 26–33. [[CrossRef](#)]
8. Wang, Z.L. Zinc Oxide Nanostructures: Growth, Properties and Applications. *J. Phys. Condens. Matter* **2004**, *16*, R829–R858. [[CrossRef](#)]
9. Klingshirn, C.F.; Meyer, B.K.; Waag, A.; Hoffmann, A.; Geurts, J. *Zinc Oxide: From Fundamental Properties towards Novel Applications*; Springer Series in Materials Science; Springer: Berlin/Heidelberg, Germany, 2010; Volume 120, ISBN 978-3-642-10576-0.
10. Janotti, A.; Van De Walle, C.G. Fundamentals of Zinc Oxide as a Semiconductor. *Rep. Prog. Phys.* **2009**, *72*, 126501. [[CrossRef](#)]
11. Ellmer, K.; Klein, A.; Rech, B. *Transparent Conductive Zinc Oxide: Basics and Applications in Thin Film Solar Cells*, 1st ed.; Springer: Berlin/Heidelberg, Germany, 2008; p. 62.
12. Siddiqi, K.S.; Ur Rahman, A.; Tajuddin; Husen, A. Properties of Zinc Oxide Nanoparticles and Their Activity Against Microbes. *Nanoscale Res. Lett.* **2018**, *13*, 141. [[CrossRef](#)]
13. Zhang, Y.; Nayak, T.; Hong, H.; Cai, W. Biomedical Applications of Zinc Oxide Nanomaterials. *Curr. Mol. Med.* **2013**, *13*, 1633–1645. [[CrossRef](#)] [[PubMed](#)]
14. Misra, S.; Wang, H. Review on the Growth, Properties and Applications of Self-Assembled Oxide–Metal Vertically Aligned Nanocomposite Thin Films—Current and Future Perspectives. *Mater. Horiz.* **2021**, *8*, 869–884. [[CrossRef](#)] [[PubMed](#)]
15. Borges, J.; Rodrigues, M.S.; Kubart, T.; Kumar, S.; Leifer, K.; Evaristo, M.; Cavaleiro, A.; Apreutesei, M.; Pereira, R.M.S.; Vasilevskiy, M.I.; et al. Thin Films Composed of Gold Nanoparticles Dispersed in a Dielectric Matrix: The Influence of the Host Matrix on the Optical and Mechanical Responses. *Thin Solid Films* **2015**, *596*, 8–17. [[CrossRef](#)]
16. Zhang, D.; Yang, S.; Zhang, X.-Y.; Ma, N.; Han, B.; Zhao, W.; Chi, S.; Liu, Y.; Yang, J.; Chen, L. Damping Resonance and Refractive Index Effect on the Layer-by-Layer Sputtering of Ag and Al<sub>2</sub>O<sub>3</sub> on the Polystyrene Template. *Spectrochim. Acta Part A Mol. Biomol. Spectrosc.* **2020**, *238*, 118430. [[CrossRef](#)] [[PubMed](#)]
17. Dang, X.; Qi, J.; Klug, M.T.; Chen, P.-Y.; Yun, D.S.; Fang, N.X.; Hammond, P.T.; Belcher, A.M. Tunable Localized Surface Plasmon-Enabled Broadband Light-Harvesting Enhancement for High-Efficiency Panchromatic Dye-Sensitized Solar Cells. *Nano Lett.* **2013**, *13*, 637–642. [[CrossRef](#)] [[PubMed](#)]
18. Sagidolda, Y.; Yergaliyeva, S.; Tolepov, Z.; Ismailova, G.; Orynbay, B.; Nemkayeva, R.; Prikhodko, O.; Peshaya, S.; Maksimova, S.; Guseinov, N.; et al. Peculiarities of the Structure of Au–TiO<sub>2</sub> and Au–WO<sub>3</sub> Plasmonic Nanocomposites. *Materials* **2023**, *16*, 6809. [[CrossRef](#)] [[PubMed](#)]
19. Chen, A.; Jia, Q. A Pathway to Desired Functionalities in Vertically Aligned Nanocomposites and Related Architectures. *MRS Bull.* **2021**, *46*, 115–122. [[CrossRef](#)]
20. MacManus-Driscoll, J.L.; Zerrer, P.; Wang, H.; Yang, H.; Yoon, J.; Fouchet, A.; Yu, R.; Blamire, M.G.; Jia, Q. Strain Control and Spontaneous Phase Ordering in Vertical Nanocomposite Heteroepitaxial Thin Films. *Nat. Mater.* **2008**, *7*, 314–320. [[CrossRef](#)]
21. Paldi, R.L.; Lu, J.; Pachaury, Y.; He, Z.; Bhatt, N.A.; Zhang, X.; El-Azab, A.; Siddiqui, A.; Wang, H. ZnO–Au<sub>x</sub>Cu<sub>1–x</sub> Alloy and ZnO–Au<sub>x</sub>Al<sub>1–x</sub> Alloy Vertically Aligned Nanocomposites for Low-Loss Plasmonic Metamaterials. *Molecules* **2022**, *27*, 1785. [[CrossRef](#)]
22. Paldi, R.L.; Qi, Z.; Misra, S.; Lu, J.; Sun, X.; Phuah, X.L.; Kalaswad, M.; Bischoff, J.; Branch, D.W.; Siddiqui, A.; et al. Nanocomposite-Seeded Epitaxial Growth of Single-Domain Lithium Niobate Thin Films for Surface Acoustic Wave Devices. *Adv. Photonics Res.* **2021**, *2*, 2000149. [[CrossRef](#)]
23. Paldi, R.L.; Sun, X.; Phuah, X.L.; Lu, J.; Zhang, X.; Siddiqui, A.; Wang, H. Deposition Pressure-Induced Microstructure Control and Plasmonic Property Tuning in Hybrid ZnO–Ag<sub>x</sub> Au<sub>1–x</sub> Thin Films. *Nanoscale Adv.* **2021**, *3*, 2870–2878. [[CrossRef](#)] [[PubMed](#)]
24. Huang, J.; Wang, H.; Qi, Z.; Lu, P.; Zhang, D.; Zhang, B.; He, Z.; Wang, H. Multifunctional Metal–Oxide Nanocomposite Thin Film with Plasmonic Au Nanopillars Embedded in Magnetic La<sub>0.67</sub>Sr<sub>0.33</sub>MnO<sub>3</sub> Matrix. *Nano Lett.* **2021**, *21*, 1032–1039. [[CrossRef](#)] [[PubMed](#)]
25. Lu, J.; Paldi, R.L.; Pachaury, Y.; Zhang, D.; Wang, H.; Kalaswad, M.; Sun, X.; Liu, J.; Phuah, X.L.; Zhang, X.; et al. Ordered Hybrid Metamaterial of La<sub>0.7</sub>Sr<sub>0.3</sub>MnO<sub>3</sub>–Au Vertically Aligned Nanocomposites Achieved on Templated SrTiO<sub>3</sub> Substrate. *Mater. Today Nano* **2021**, *15*, 100121. [[CrossRef](#)]
26. Paldi, R.L.; Wang, X.; Sun, X.; He, Z.; Qi, Z.; Zhang, X.; Wang, H. Vertically Aligned Ag<sub>x</sub> Au<sub>1–x</sub> Alloyed Nanopillars Embedded in ZnO as Nanoengineered Low-Loss Hybrid Plasmonic Metamaterials. *Nano Lett.* **2020**, *20*, 3778–3785. [[CrossRef](#)] [[PubMed](#)]
27. Paldi, R.L.; Sun, X.; Wang, X.; Zhang, X.; Wang, H. Strain-Driven In-Plane Ordering in Vertically Aligned ZnO–Au Nanocomposites with Highly Correlated Metamaterial Properties. *ACS Omega* **2020**, *5*, 2234–2241. [[CrossRef](#)] [[PubMed](#)]
28. Harrington, G.F.; Santiso, J. Back-to-Basics Tutorial: X-Ray Diffraction of Thin Films. *J. Electroceram.* **2021**, *47*, 141–163. [[CrossRef](#)]
29. Kaushal, S.; Nanda, S.S.; Yi, D.K.; Ju, H. Effects of Aspect Ratio Heterogeneity of an Assembly of Gold Nanorod on Localized Surface Plasmon Resonance. *J. Phys. Chem. Lett.* **2020**, *11*, 5972–5979. [[CrossRef](#)] [[PubMed](#)]

30. Zheng, J.; Cheng, X.; Zhang, H.; Bai, X.; Ai, R.; Shao, L.; Wang, J. Gold Nanorods: The Most Versatile Plasmonic Nanoparticles. *Chem. Rev.* **2021**, *121*, 13342–13453. [[CrossRef](#)]
31. Hu, S.; Shi, W.; Chen, Y.; Chen, Y.; Liu, G.-S.; Chen, L.; Luo, Y.; Chen, Z. Dispersion Management for Hyperbolic-Metamaterials Based Surface Plasmon Resonance Sensor Towards Extremely High Sensitivity. *J. Light. Technol.* **2022**, *40*, 887–893. [[CrossRef](#)]
32. Guo, Z.; Jiang, H.; Chen, H. Hyperbolic Metamaterials: From Dispersion Manipulation to Applications. *J. Appl. Phys.* **2020**, *127*, 071101. [[CrossRef](#)]
33. Chamorro, W.; Ghanbaja, J.; Battie, Y.; Naciri, A.E.; Soldera, F.; Mücklich, F.; Horwat, D. Local Structure-Driven Localized Surface Plasmon Absorption and Enhanced Photoluminescence in ZnO-Au Thin Films. *J. Phys. Chem. C* **2016**, *120*, 29405–29413. [[CrossRef](#)]
34. Shekhar, P.; Atkinson, J.; Jacob, Z. Hyperbolic Metamaterials: Fundamentals and Applications. *Nano Converg.* **2014**, *1*, 14. [[CrossRef](#)] [[PubMed](#)]
35. Ferrari, L.; Wu, C.; Lepage, D.; Zhang, X.; Liu, Z. Hyperbolic Metamaterials and Their Applications. *Prog. Quantum Electron.* **2015**, *40*, 1–40. [[CrossRef](#)]

**Disclaimer/Publisher’s Note:** The statements, opinions and data contained in all publications are solely those of the individual author(s) and contributor(s) and not of MDPI and/or the editor(s). MDPI and/or the editor(s) disclaim responsibility for any injury to people or property resulting from any ideas, methods, instructions or products referred to in the content.